Research Article | Vol. 28, No. 21 / 12 October 2020 / Optics Express 31584
Optics EXPRESS

Influence of longitudinal mode components on second harmonic generation in III-V-on-insulator nanowires

CHARLES CIRET,[1,*] KOEN ALEXANDER,[2,3] NICOLAS POULVELLARIE,[2,3,4] MAXIMILIEN BILLET,[2,3,4] CARLOS MAS ARABI,[4] BART KUYKEN,[2,3] SIMON-PIERRE GORZA,[4] AND FRANÇOIS LEO[4]

[1]*Laboratoire de Photonique d'Angers EA 4464, Université d'Angers, Angers, France*
[2]*Photonics Research Group, Ghent University-IMEC, Ghent, Belgium*
[3]*Center for Nano- and Biophotonics (NB-Photonics), Ghent University, Ghent, Belgium*
[4]*OPERA-Photonique, Université libre de Bruxelles, Brussels, Belgium*
[*]*charles.ciret@univ-angers.fr*

Abstract: The large index contrast and the subwalength tranverse dimensions of nanowires induce strong longitudinal electric field components. We show that these components play an important role for second harmonic generation in III-V wire waveguides. To illustrate this behavior, an efficiency map of nonlinear conversion is determined based on full-vectorial calculations. It reveals that many different waveguide dimensions and directions are suitable for efficient conversion of a fundamental quasi-TE pump mode around the 1550 nm telecommunication wavelength to a higher-order second harmonic mode.

1. Introduction

The first demonstration of second harmonic generation (SHG) in 1961 paved the way for decades of research on nonlinear optics [1]. The quest for efficient conversion is still relevant today as key regions of the electromagnetic spectrum lack suitable laser sources. Other applications such as squeezed light generation [2], entangled photon generation [3] or frequency comb stabilization [4] would also benefit from efficient frequency converters.

The advent of integrated photonic platforms the last decade revolutionized frequency conversion. The large nonlinear coefficients as well as the high index contrast inherent to integrated photonics allows for strong nonlinear interaction at low power. Many instances of integrated second harmonics generation have been reported, with novel, low-loss, $LiNbO_3$ on insulator and III-V-on insulator platforms currently holding the record normalized conversion efficiency in nanowires [5–7]. In most theoretical analysis, the light is approximated by a purely transverse mode such that a single incoming polarization state and spatial profile is considered. In practice however, more complex nonlinear wave mixing can be expected because the optical modes in high index contrast waveguides display large longitudinal components. We recently experimentally demonstrated SHG enabled by longitudinal components in III-V wire waveguides [8]. Here we further investigate the impact of strong longitudinal components on SHG. We derive the ordinary differential equations describing the nonlinear coupling of a fundamental wave at ω_0 to its second harmonic (SH) at $2\omega_0$ in a III-V waveguide using full-vectorial calculations [9–15]. We identify ultra-efficient conversion for a wide range of waveguide dimensions and highlight the major role played by the propagation direction.

While we focus on III-V semiconductor wire waveguides [6,7,16], we stress that our analysis can be easily adapted to other platforms. We consider indium gallium phosphide (InGaP) around 1550 nm as the guiding material [8,17]. InGaP displays a $\bar{4}$ symmetry and exhibits very low nonlinear losses at telecom wavelengths in the C-band. The $\chi^{(2)}_{xyz}$ coefficient, which is the only

#402150 https://doi.org/10.1364/OE.402150
Journal © 2020 Received 10 Jul 2020; revised 11 Sep 2020; accepted 12 Sep 2020; published 6 Oct 2020

Optics EXPRESS

nonzero tensor element, was measured to be as high as 220 pm/V around 1550 nm [18]. Because of the lack of birefringence in III-V semiconductors, several different approaches have been implemented to achieve phase matching, including form birefringence [19], quasi-phase-matching [20–24] and modal phase matching [6,25]. Our theoretical study is focused on the latter.

The paper is organized as follows. In Section 2, we recall the general formalism used for describing bound modes and the derivation of the first order differential equation modeling their nonlinear coupling. Specifically, we resort to a perturbative method to include second order nonlinearities. In Section 3, we apply the formalism to SHG. In Section 4, we discuss the influence of the propagation direction on the conversion efficiency and present the efficiency map for the specific case of InGaP-on insulator waveguides. Concluding remarks are given in Section 5.

2. General framework

2.1. Linear waveguides

We start by discussing the properties of bound modes in a lossless linear waveguide [26]. We consider a III-V-on-insulator wire waveguide as shown in the inset of Fig. 1. An electromagnetic wave oscillating at a frequency ω propagating in the waveguide must satisfy the source-free linear Maxwell equations which read in the Fourier domain:

$$\nabla \times \tilde{\mathbf{E}}_0(\mathbf{r},\omega) = i\omega\mu_0\tilde{\mathbf{H}}_0(\mathbf{r},\omega), \tag{1a}$$

$$\nabla \times \tilde{\mathbf{H}}_0(\mathbf{r},\omega) = -i\omega\epsilon_0[n(\mathbf{r}_\perp)]^2\tilde{\mathbf{E}}_0(\mathbf{r},\omega), \tag{1b}$$

$$\nabla \cdot [[n(\mathbf{r}_\perp)]^2\tilde{\mathbf{E}}_0(\mathbf{r},\omega)] = 0, \tag{1c}$$

$$\nabla \cdot \tilde{\mathbf{H}}_0(\mathbf{r},\omega) = 0. \tag{1d}$$

$\tilde{\mathbf{E}}_0(\mathbf{r},\omega)$ and $\tilde{\mathbf{H}}_0(\mathbf{r},\omega)$ are called the unperturbed fields. They represent the electromagnetic fields of a continuous wave or a narrowband pulse for which the dispersion, loss and nonlinearity terms are zero. $n(\mathbf{r}_\perp)$ is the local refractive index of the unperturbed waveguide cross-section. $\tilde{\mathbf{E}}_0, \tilde{\mathbf{H}}_0$ are related to their time counterpart through the Fourier transformation :

$$\mathbf{G}(\mathbf{r},t) = \frac{1}{2\pi}\int_{-\infty}^{+\infty}\tilde{\mathbf{G}}(\mathbf{r},\omega)e^{-i\omega t}d\omega, \tag{2}$$

where, $\mathbf{G} = \mathbf{E}_0$ or $\mathbf{H}_0$.

The translational invariance along the propagation axis allows to write the j^{th} guided mode as a spatial distribution depending on the transversal coordinates of the electric and magnetic fields with a fixed propagation constant. They read:

$$\tilde{\mathbf{E}}_{0,j}(\mathbf{r},\omega) = a_{0,j}\frac{\mathbf{e}_j(\mathbf{r}_\perp,\omega)}{\sqrt{N_j}}e^{i\beta_j z}, \tag{3}$$

$$\tilde{\mathbf{H}}_{0,j}(\mathbf{r},\omega) = a_{0,j}\frac{\mathbf{h}_j(\mathbf{r}_\perp,\omega)}{\sqrt{N_j}}e^{i\beta_j z}, \tag{4}$$

where $\mathbf{e}_j(\mathbf{r}_\perp,\omega)$ and $\mathbf{h}_j(\mathbf{r}_\perp,\omega)$ are the vectorial electric and magnetic mode profiles. $a_{0,j}$ is the complex amplitude of the mode and β_j is the mode propagation constant. N_j is the mode

Optics EXPRESS

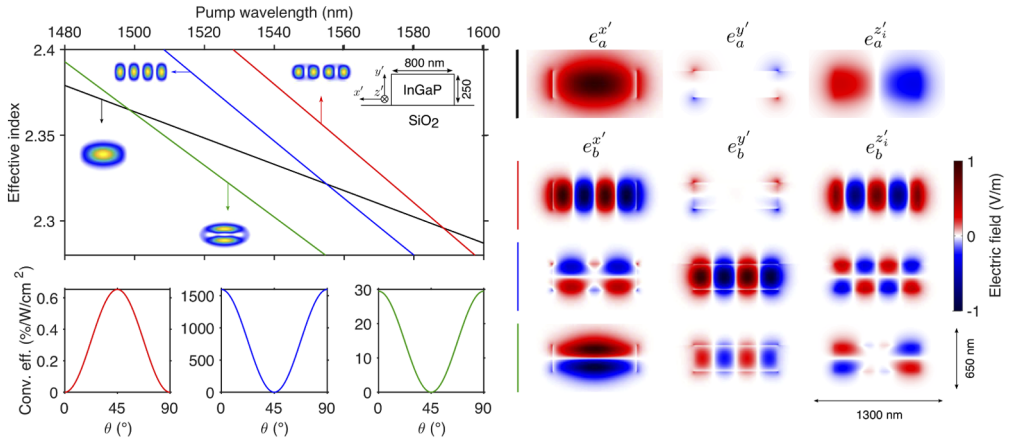

Fig. 1. Top left: Effective indices of a fundamental quasi-TE_{00} pump mode and three different SH higher-order modes of a 250 nm high, 800 nm wide InGaP waveguide. The corresponding Poynting vector distributions are shown as inset. Bottom left: Theoretical conversion efficiency as a function of the propagation angle in the (010) crystal plane for the three phase matching points. Right: Spatial profiles of each component of the fundamental and SH modes.

normalization, defined by:

$$N_j(\omega) = \frac{1}{2}\left|\int \mathbf{e}_j(\mathbf{r}_\perp,\omega)\times\mathbf{h}_j^*(\mathbf{r}_\perp,\omega)\cdot\hat{\mathbf{z}}dA\right|. \tag{5}$$

The mode orthogonality condition reads:

$$\frac{1}{2}\int\{\frac{\mathbf{e}_j(\mathbf{r}_\perp,\omega)}{\sqrt{N_j}}\times\frac{\mathbf{h}_i^*(\mathbf{r}_\perp,\omega)}{\sqrt{N_i}}\}\cdot\hat{\mathbf{z}}dA = \delta_{ij}, \tag{6}$$

where the integration area is transverse to the propagation plane and $\hat{\mathbf{z}}$ is the unit vector in the propagation direction z. The mode construction and normalization ensures that $|a_{0,j}|^2 \equiv P_j$, where P_j is the total power propagating in the j^{th} mode. We refer the reader to [26] for more information on the mode field distributions and their relation to one another. In this paper, the modes and the propagation constants are computed by use of a commercial mode solver (Lumerical). Yet we recall a couple of points that will play a role in the analysis of the nonlinear coupling: (i) The longitudinal electric field component of a mode has a phase difference of $\pi/2$ with the corresponding transverse components and (ii), because of the symmetry of the index profile in the horizontal direction (see the inset of Fig. 1), the longitudinal and vertical electric field components display the opposite parity as the one of the horizontal component. Here we consider airclad waveguides such that there is only one symmetry plane (yz-plane). A few examples of the spatial distribution of the electric fields are shown in Fig. 1. Modes whose main component, the one with the strongest local electric field, is horizontal (resp. vertical) are labeled TE_{lk} (resp. TM_{lk}), where l and k are the number of zeros of the Poynting vector in the horizontal and vertical directions [27].

2.2. Nonlinear coupling

We next derive the expressions for the nonlinear coupling between different forward propagating modes. In this derivation, the nonlinearity is treated as a perturbation to the ideal lossless linear

Optics EXPRESS

waveguide [9–15]. The perturbed waveguide modes are written in the Fourier domain as:

$$\tilde{\mathbf{E}}_{\mathbf{j}}(\mathbf{r},\omega) = a_j(z)\frac{\mathbf{e}_j(\mathbf{r}_\perp,\omega)}{\sqrt{N_j}}e^{i\beta_j z}, \tag{7}$$

$$\tilde{\mathbf{H}}_{\mathbf{j}}(\mathbf{r},\omega) = a_j(z)\frac{\mathbf{h}_j(\mathbf{r}_\perp,\omega)}{\sqrt{N_j}}e^{i\beta_j z}. \tag{8}$$

where $a_j(z)$ is the complex slowly varying amplitudes. In what follows, we consider the guided wave to be a superposition of a finite number of single frequency bound modes. To simplify the notations, we map the two sets of discrete values for the modes and the frequencies to the subscript q. In the time domain, the fields read:

$$\mathbf{E}(\mathbf{r},t) = \sum_q \Re\{a_q(z)\frac{\mathbf{e}_q(\mathbf{r}_\perp,\omega_q)}{\sqrt{N_q}}e^{i(\beta_q z-\omega_q t)}\}, \tag{9}$$

$$\mathbf{H}(\mathbf{r},t) = \sum_q \Re\{a_q(z)\frac{\mathbf{h}_q(\mathbf{r}_\perp,\omega_q)}{\sqrt{N_q}}e^{i(\beta_q z-\omega_q t)}\}. \tag{10}$$

These fields obey the Maxwell curl equations including the nonlinear polarization oscillating at ω, $\tilde{\mathbf{P}}^{NL}(\omega)$,

$$\nabla\times\tilde{\mathbf{E}}(\mathbf{r},\omega) = i\omega\mu_0\tilde{\mathbf{H}}(\mathbf{r},\omega), \tag{11}$$

$$\nabla\times\tilde{\mathbf{H}}(\mathbf{r},\omega) = -i\omega\epsilon_0 n^2\tilde{\mathbf{E}}(\mathbf{r},\omega) - i\omega\tilde{\mathbf{P}}^{NL}(\mathbf{r},\omega). \tag{12}$$

To derive the coupled-wave equations, we make use of the conjugated form of the Lorentz reciprocity theorem [26]:

$$\int \nabla\cdot\mathbf{F}dA = \frac{\partial}{\partial z}\int \mathbf{F}\cdot\hat{\mathbf{z}}dA. \tag{13}$$

The $\mathbf{F}$-field can be constructed from the perturbed and unperturbed waveguide mode fields at ω_q as $\mathbf{F} \equiv \tilde{\mathbf{E}}^*_{0,q}(\mathbf{r},\omega_q)\times\tilde{\mathbf{H}}(\mathbf{r},\omega_q) + \tilde{\mathbf{E}}(\mathbf{r},\omega_q)\times\tilde{\mathbf{H}}^*_{0,q}(\mathbf{r},\omega_q)$. Substituting this in Eq. (13) yields:

$$\begin{aligned}\int \{&(\nabla\times\tilde{\mathbf{E}}^*_{0,q}(\mathbf{r},\omega_q))\cdot\tilde{\mathbf{H}}(\mathbf{r},\omega_q) - \tilde{\mathbf{E}}^*_{0,q}(\mathbf{r},\omega_q)\cdot(\nabla\times\tilde{\mathbf{H}}(\mathbf{r},\omega_q))\\ &+ (\nabla\times\tilde{\mathbf{E}}(\mathbf{r},\omega_q))\cdot\tilde{\mathbf{H}}^*_{0,q}(\mathbf{r},\omega_q) - \tilde{\mathbf{E}}(\mathbf{r},\omega_q)\cdot(\nabla\times\tilde{\mathbf{H}}^*_{0,q}(\mathbf{r},\omega_q))\}dA\\ &= \frac{\partial}{\partial z}\int\frac{a^*_{0,q}a_q(z)}{N_q}\{\mathbf{e}_q(\mathbf{r}_\perp,\omega_q)\times\mathbf{h}^*_q(\mathbf{r}_\perp,\omega_q) + \mathbf{e}^*_q(\mathbf{r}_\perp,\omega_q)\times\mathbf{h}_q(\mathbf{r}_\perp,\omega_q))\}\cdot\hat{\mathbf{z}}dA.\end{aligned} \tag{14}$$

The left-hand side of Eq. (14) can be simplified by substituting Eqs. (1a–(1b) and Eqs. (11)–(12), and the right-hand side by using the normalization condition [Eq. (5)]. This gives:

$$\frac{d}{dz}a_q = i\omega_q\frac{e^{-i\beta_q z}}{4\sqrt{N_q}}\int\mathbf{e}^*_q(\mathbf{r}_\perp,\omega_q)\cdot\tilde{\mathbf{P}}^{NL}(\mathbf{r},\omega_q)dA, \tag{15}$$

which describes the evolution of the amplitude of mode q along the waveguide.

3. Second-harmonic generation

We apply the formalism from the previous section to the specific case of SHG. For simplicity we only consider type I phase matching. The fundamental wave, with a carrier frequency ω_0, and

Optics EXPRESS

the second harmonic, with a carrier frequency $2\omega_0$, are each limited to a single spatial mode. The total electric and magnetic fields are:

$$\mathbf{E}(\mathbf{r},t) = \Re\{a(z)\frac{\mathbf{e}_a(\omega_0,\mathbf{r}_\perp)}{\sqrt{N_a}}e^{i(\beta_a z-\omega_0 t)} + b(z)\frac{\mathbf{e}_b(2\omega_0,\mathbf{r}_\perp)}{\sqrt{N_b}}e^{i(\beta_b z-2\omega_0 t)}\}, \tag{16}$$

$$\mathbf{H}(\mathbf{r},t) = \Re\{a(z)\frac{\mathbf{h}_a(\omega_0,\mathbf{r}_\perp)}{\sqrt{N_a}}e^{i(\beta_a z-\omega_0 t)} + b(z)\frac{\mathbf{h}_b(2\omega_0,\mathbf{r}_\perp)}{\sqrt{N_b}}e^{i(\beta_b z-2\omega_0 t)}\}, \tag{17}$$

By injecting the fields in Eq. (13) and following the same development as before, one finds the following coupled ordinary differential equation describing the nonlinear coupling between the two modes:

$$\frac{da(z)}{dz} = i\omega_0\frac{e^{-i\beta_a z}}{4\sqrt{N_a}}\int \mathbf{e}_a^*\cdot\tilde{\mathbf{P}}^{NL}(\mathbf{r},\omega_0)dA, \tag{18a}$$

$$\frac{db(z)}{dz} = i2\omega_0\frac{e^{-i\beta_b z}}{4\sqrt{N_b}}\int \mathbf{e}_b^*\cdot\tilde{\mathbf{P}}^{NL}(\mathbf{r},2\omega_0)dA. \tag{18b}$$

In the time domain, the nonlinear polarization reads:

$$\mathbf{P}^{NL}(\mathbf{r},t) = \Re\{\tilde{\mathbf{P}}^{NL}(\mathbf{r},\omega_0)e^{-i\omega_0 t} + \tilde{\mathbf{P}}^{NL}(\mathbf{r},2\omega_0)e^{-i2\omega_0 t} + \cdots\} \tag{19}$$

We here focus on a purely quadratic nonlinearity. By assuming a local response, we can write:

$$\mathbf{P}^{NL}(\mathbf{r},t) = \varepsilon_0\iint \underline{\underline{\chi}}^{(2)}(\mathbf{r},t_1,t_2):\mathbf{E}(\mathbf{r},t-t_1)\mathbf{E}(\mathbf{r},t-t_2)dt_1dt_2. \tag{20}$$

We now insert the electric field of Eq. (16) in Eq. (20) and find:

$$\tilde{\mathbf{P}}^{NL}(\mathbf{r},\omega_0) = \frac{b(z)a^*(z)}{\sqrt{N_aN_b}}\varepsilon_0\underline{\underline{\chi}}^{(2)}(\mathbf{r},\omega_0;2\omega_0,-\omega_0):\mathbf{e}_b\mathbf{e}_a^*e^{i(\beta_b-\beta_a)z}, \tag{21a}$$

$$\tilde{\mathbf{P}}^{NL}(\mathbf{r},2\omega_0) = \frac{1}{2}\frac{a^2(z)}{N_a}\varepsilon_0\underline{\underline{\chi}}^{(2)}(\mathbf{r},2\omega_0;\omega_0,\omega_0):\mathbf{e}_a\mathbf{e}_a e^{i2\beta_a z}, \tag{21b}$$

where we introduced the commonly used Fourier components of the nonlinear tensor. By injecting these expressions in Eqs. (18a) and (18b), we find:

$$\frac{da(z)}{dz} = \frac{i\omega_0\varepsilon_0}{4}\frac{b(z)a^*(z)e^{i(\beta_b-2\beta_a)z}}{N_a\sqrt{N_b}}\int\sum_{jkl}\chi^{(2)}_{jkl}e_a^{*j}e_b^k e_a^{*l}dA, \tag{22a}$$

$$\frac{db(z)}{dz} = \frac{i\omega_0\varepsilon_0}{4}\frac{a^2(z)e^{i(2\beta_a-\beta_b)z}}{N_a\sqrt{N_b}}\int\sum_{jkl}\chi^{(2)}_{jkl}e_b^{*j}e_a^k e_a^{l}dA, \tag{22b}$$

where we expanded the tensor product $(j,k,l=x,y,z)$ and set $\underline{\underline{\chi}}^{(2)}(\mathbf{r},\omega_0;2\omega_0,-\omega_0) = \underline{\underline{\chi}}^{(2)}(\mathbf{r},2\omega_0;\omega_0,\omega_0) = \underline{\underline{\chi}}^{(2)}$.

We define the effective nonlinear coefficient as:

$$\kappa = \frac{\omega_0\varepsilon_0}{4N_a\sqrt{N_b}}\int\sum_{jkl}\chi^{(2)}_{jkl}e_b^{*j}e_a^k e_a^l dA, \tag{23}$$

such that Eqs. (22a) and (22b) become

$$\frac{da(z)}{dz} = i\kappa^* b(z)a^*(z)e^{-i\Delta\beta z}, \tag{24a}$$

$$\frac{db(z)}{dz} = i\kappa a^2(z)e^{i\Delta\beta z}. \tag{24b}$$

where $\Delta\beta = 2\beta_a - \beta_b$. In the literature, SHG is often characterized by the undepleted theoretical conversion efficiency $P_{2\omega_0}(L)/(P_{\omega_0}(0)L)^2$ expressed in %/(Wm^2) where L is the length of the

Optics EXPRESS

waveguide. By plugging the initial conditions $a(0) = \sqrt{P_{\omega_0}(0)}, b(0) = 0$ in Eq. (24b), integrating over the length of the waveguide and neglecting pump depletion (as well as propagation loss), we obtain:

$$P_{2\omega_0}(L) = |\kappa|^2 P_{\omega_0}^2(0) L^2 \mathrm{sinc}^2(\Delta\beta L/2). \tag{25}$$

In the case of perfect phase matching ($\Delta\beta = 0$), Eq. (25) becomes $P_{2\omega_0}(L)/(P_{\omega_0}(0)L)^2 = |\kappa|^2$. In what follows, we use the theoretical conversion efficiency $|\kappa|^2$ to characterize SHG. Note that, Eq. (25) can be easily generalized to include the impact of propagation loss on the second harmonic generation efficiency [8].

4. Application to III-V-on-insulator wire waveguides

We now focus on the specific case of III-V-on insulator wire waveguides. Because the propagation direction is not fixed in the crystal frame (xyz), we introduce the coordinates ($x'y'z'$) to describe the optical wave in the waveguide frame. The propagation Eqs. (24a) and (24b), simply become:

$$\frac{da(z')}{dz'} = i\kappa^* b(z') a^*(z') e^{-i\Delta\beta z'}, \tag{26a}$$

$$\frac{db(z')}{dz'} = i\kappa a^2(z') e^{i\Delta\beta z'}. \tag{26b}$$

Most III-V wafers are grown along a crystallographic axis. Consequently, we may consider that the light propagates in the xz-plane (010) of the crystal. The two coordinate frames are linked through the rotation matrix:

$$\begin{pmatrix} x \\ y \\ z \end{pmatrix} = \begin{pmatrix} \cos\theta & 0 & -\sin\theta \\ 0 & 1 & 0 \\ \sin\theta & 0 & \cos\theta \end{pmatrix} \begin{pmatrix} x' \\ y' \\ z' \end{pmatrix}, \tag{27}$$

where θ is the angle between the propagation direction z' and the z axis [8]. The zinc-blende crystalline arrangement of III-V crystals leads to a single nonzero tensor element ($\chi^{(2)}_{xyz} = 2d_{14} \neq 0$). In that case the tensor product in Eq. (23) becomes:

$$\begin{aligned} \sum_{jkl} \chi^{(2)}_{jkl} e_b^{*j} e_a^k e_a^l &= \chi^{(2)}_{xyz} e_b^{*x} e_a^y e_a^z + \chi^{(2)}_{xzy} e_b^{*x} e_a^z e_a^y \\ &+ \chi^{(2)}_{yxz} e_b^{*y} e_a^x e_a^z + \chi^{(2)}_{yzx} e_b^{*y} e_a^z e_a^x \\ &+ \chi^{(2)}_{zxy} e_b^{*z} e_a^x e_a^y + \chi^{(2)}_{zyx} e_b^{*z} e_a^y e_a^x \\ &= 2\chi^{(2)}_{xyz} \left(e_b^{*x} e_a^y e_a^z + e_b^{*y} e_a^x e_a^z + e_b^{*z} e_a^x e_a^y \right), \end{aligned} \tag{28}$$

where the second step is a consequence of the Kleinman symmetry condition [28]. The general form of the effective nonlinearity in the crystal reference frame hence reads:

$$\kappa = \frac{\omega_0 \varepsilon_0}{2N_a\sqrt{N_b}} \int_{wg} \chi^{(2)}_{xyz} \left(e_b^{*x} e_a^y e_a^z + e_b^{*y} e_a^x e_a^z + e_b^{*z} e_a^x e_a^y \right) dA, \tag{29}$$

where the integration area is limited to the InGaP core waveguide. In the waveguide frame it becomes:

$$\begin{aligned} \kappa = \frac{\omega_0 \varepsilon_0}{2N_a\sqrt{N_b}} \int \chi^{(2)}_{xyz} \Big[&\left(e_b^{*x'} \cos\theta - e_b^{*z'} \sin\theta \right) \left(e_a^{y'} \right) \left(e_a^{x'} \sin\theta + e_a^{z'} \cos\theta \right) \\ &+ \left(e_b^{*y'} \right) \left(e_a^{x'} \cos\theta - e_a^{z'} \sin\theta \right) \left(e_a^{x'} \sin\theta + e_a^{z'} \cos\theta \right) \\ &+ \left(e_b^{*x'} \sin\theta + e_b^{*z'} \cos\theta \right) \left(e_a^{y'} \right) \left(e_a^{x'} \cos\theta - e_a^{z'} \sin\theta \right) \Big] dA. \end{aligned} \tag{30}$$

Optics EXPRESS

We next evaluate the theoretical converison efficiency in specific waveguides. We start by investigating a 800 nm wide, 250 nm thick InGaP-on-insulator wire waveguide. We use the material dispersion reported in [29] to compute the effective index and spatial distributions of the optical modes. We limit ourselves to SHG of a fundamental quasi-transverse electric mode (TE_{00}) and start with the dimensions of waveguides recently used for supercontinuum generation [30]. Figure 1 displays the indices of the fundamental TE mode around the pump wavelength and of several higher-order modes around the SH wavelength. The corresponding spatial distributions of the electric fields are also shown. Note that the vectorial nature of the fields stands out in the figure as the longitudinal and transverse components of the SH modes have comparable magnitudes. Several phase matching points, indicated by a crossing between the pump mode and a SH mode, are found. The effective nonlinearity associated with each phase matching can be evaluated through Eq. (30). The dependence of the conversion efficiency $|\kappa|^2$ with θ (also shown in Fig. 1) reflects the $\bar{4}$ symmetry of the material. As we here focus on straight waveguides, we simply look for the angle that maximizes conversion between two modally phase matched waves. Interestingly, it depends on the symmetry of the spatial distributions of the modes. The conversion to the TE_{30} mode is maximum when $\theta = 45°$ while the conversion to the TM_{30} and and TE_{01} modes, is optimized when $\theta = 0°$. More generally, we only find maxima at 0° and 45° and hence focus on those two angles.

The 45° effective nonlinearity reads:

$$\kappa(45°) = \frac{\omega_0 \varepsilon_0}{2N_a\sqrt{N_b}} \int \chi^{(2)}_{xyz} \left[e_a^{y'} \left(e_b^{x'} e_a^{x'} - e_b^{z'_i} e_a^{z'_i} \right) + \frac{e_b^{y'}}{2} \left(e_a^{x'2} + e_a^{z'_i 2} \right) \right] dA, \tag{31}$$

where we introduced the spatial distribution $e^{z'_i}_{a,b} = -ie^{z'}_{a,b}$ corresponding to the imaginary part of the longitudinal component. Most previous results of SHG in III-V nanowaveguides were performed in this configuration. This is likely because the cleave directions for III-V semiconductors grown on (100) substrate are [110] and [1$\bar{1}$0]. Waveguides whose cleaved facets are perpendicular to the propagation direction are hence oriented 45° with respect to the crystal axis. For example, ultra efficient conversion was recently demonstrated in that direction in gallium arsenide wire waveguides [6], where a quasi-TE pump is coupled to a quasi-TM SH mode. In that case, it is the $e_b^{y'} e_a^{x'2}$ term that dominates such that a scalar approximation suffices to predict the nonlinear coupling. Here however, we find conversion to a TE_{30} mode whose vertical component is weak such that no single term in Eq. (31) dominates. This highlights the importance of a full-vectorial approach, which takes into account transverse and longitudinal components of the modes, to accurately model the nonlinear frequency conversion, even in a 45° waveguide.

The 0° effective nonlinearity, on the other hand, reads:

$$\kappa(0°) = \frac{i\omega_0 \varepsilon_0}{2N_a\sqrt{N_b}} \int \chi^{(2)}_{xyz} \left(e_b^{x'} e_a^{y'} e_a^{z'_i} + e_b^{y'} e_a^{x'} e_a^{z'_i} - e_b^{z'_i} e_a^{x'} e_a^{y'} \right) dA. \tag{32}$$

Nonlinear coupling in this case always involves a longitudinal mode component [8]. In both nonlinear coefficients involving the TM_{30} and TE_{01} modes shown in Fig. 1, it is the $(e_b^{y'} e_a^{x'} e_a^{z'_i})$ term that dominates, as can be expected from using a quasi-TE pump. Interestingly the y' component of these SH modes are similar despite the modes having very different Poynting vector distributions. The more efficient conversion is logically found when most of the energy is carried by the vertical electric field component.

The main difference between 0° and 45° oriented waveguides stems from the profiles of the excited modes. As a reminder there is a single, vertical, symmetry plane. Consequently, only the parity of the profiles along the x' direction matters. In a 45° waveguide, the y' component of the SH mode must be symmetric as the fundamental components are squared [see Eq. (31)].

Optics EXPRESS

Conversely, in 0° waveguides, only SH modes with an antisymmetric vertical component will be excited because the product of the transverse and longitudinal components of the pump is always antisymmetric. We stress that these considerations are valid for type I SHG, irrespective of the pump mode.

Importantly, we find that III-V nanowaveguides are suitable for efficient conversion in both propagation orientations.

Next we study the impact of the waveguide dimensions on the SHG efficiency when considering a fundamental mode wavelength around 1550 nm. Specifically, we vary the width and height of the III-V section and look for phase matching between a fundamental quasi-TE mode and a SH higher-order mode in a 10 nm window around 1550 nm. For each instance of phase matching, we compute the effective nonlinearity for different propagation directions and store only the maximum coefficient. Due to the symmetry of the crystal, we limit ourselves to the first quadrant. We investigate waveguides with a width between 600 nm and 1000 nm and a height between 50 nm and 350 nm. To limit the computational time, we use a resolution of 5 nm. Every phase matching point is shown as a marker in Fig. 2. The marker color codes the strength of the coupling and its shape indicates the angle between the waveguide and the crystal axis that maximizes the interaction. Squares are used for the 0° waveguides while diamonds represent 45° waveguides. To highlight similar interactions, we evaluate the overlap between neighboring markers via Eq. (5). We define a threshold at 70%, beyond which we infer it is the same mode and connect the two markers with a line. We identify 8 independent modes. Their Poynting vector distribution is shown in Fig. 2. The maximum effective nonlinearity [$\kappa = 2816\ (\sqrt{\mathrm{W}}\mathrm{m})^{-1}$] is found for a waveguide with a width of 810 nm and a height of 110 nm, directed at 45°. The SH propagates in a TM_{00} mode and the corresponding conversion efficiency is as high as 79300 %/(Wcm^2). This interaction is well-known as it is mostly due to the mixing of the transverse components of the modes [6]. More interesting are the many square markers indicating coupling enabled by longitudinal components. The maximum conversion efficiency [52350 %/(Wcm^2)], found for a TM_{10} mode, is predicted to be almost as efficient as the conversion to a TM_{00} mode. Moreover, we find that the phase matching is more sensitive to width variations in the latter. In waveguides with a thickness of 200 nm or more, it is the 0° configuration that is the most efficient. These thicknesses are commonly used as they lead to lower propagation losses than in thinner

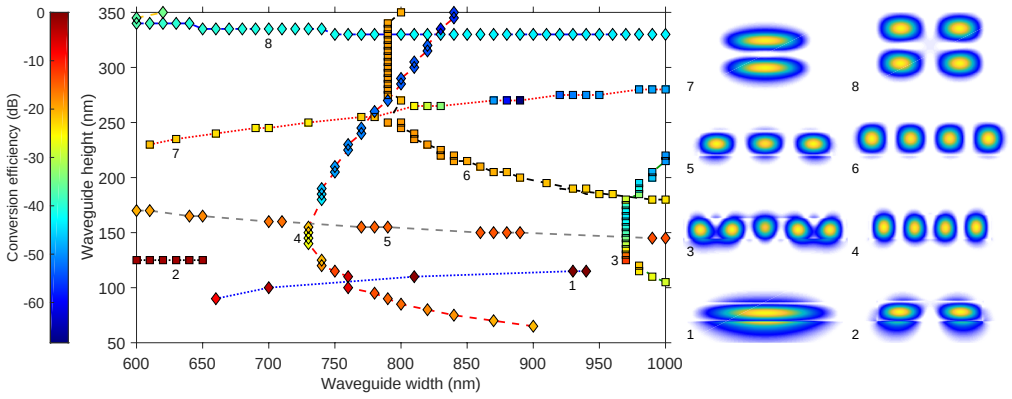

Fig. 2. Left: Efficiency map of the nonlinear coupling between a TE_{00} pump mode and a higher-order SH mode. Only phase-matched interactions are shown. Diamond (resp. square) markers correspond to 45° (resp. 0°) waveguides. The lines connect neighboring points corresponding to the same higher-order mode. Right: Poynting vector distribution of the eight independent SH modes found in the map.

Optics EXPRESS

layers [31,32]. Importantly, these highly efficient geometries could not be predicted using a scalar approach.

We stress that not all possible couplings are shown in Fig. 2. We use a 5 nm resolution and wave vectors are very sensitive to waveguide dimensions. Also, quasi-phase-matching can be used to efficiently couple two modes with different effective indices [33]. Yet, many of the novel nonlinear couplings we show here are predicted to be very efficient. We expect them to play a significant role in future integrated wavelength converters.

5. Conclusion

We have theoretically investigated SHG in III-V semiconductor wire waveguides. By using a full-vectorial model we found many instances of efficient conversion between a fundamental pump mode and a higher-order SH mode. Our results highlight the crucial role played by the longitudinal component of the electric field. When propagating along the crystal axis, only wave mixing involving different components is permitted by the single nondiagonal $\chi^{(2)}_{xyz}$ element. Due the high index contrast, the longitudinal electric field component can be almost as large as its transverse counterpart [34] making this configuration very efficient.

Funding

European Research Council (757800, 759483); Conseil Régional des Pays de la Loire (Paris-Scientifique "Nano-Light").

Acknowledgements

This work was supported by funding from the European Research Council (ERC) under the European Unions Horizon 2020 research and innovation programme (grant agreement Nos 759483 & 757800) and by the Fonds de la Recherche Fondamentale Collective (grant agreement No PDR.T.0185.18). CC acknowledges the financial support from Région Pays de la Loire through the grant Paris Scientifique "Nano-Light."

Disclosures

The authors declare no conflicts of interest.

References

1. P. A. Franken, A. E. Hill, C. W. Peters, and G. Weinreich, "Generation of Optical Harmonics," Phys. Rev. Lett. **7**(4), 118–119 (1961).
2. R. Paschotta, M. Collett, P. Kurz, K. Fiedler, H. A. Bachor, and J. Mlynek, "Bright squeezed light from a singly resonant frequency doubler," Phys. Rev. Lett. **72**(24), 3807–3810 (1994).
3. X. Guo, C. Zou, C. Schuck, H. Jung, R. Cheng, and H. X. Tang, "Parametric down-conversion photon-pair source on a nanophotonic chip," Light: Sci. Appl. **6**(5), e16249 (2017).
4. R. Holzwarth, T. Udem, T. W. Hänsch, J. C. Knight, W. J. Wadsworth, and P. St. J. Russell, "Optical Frequency Synthesizer for Precision Spectroscopy," Phys. Rev. Lett. **85**(11), 2264–2267 (2000).
5. C. Wang, C. Langrock, A. Marandi, M. Jankowski, M. Zhang, B. Desiatov, M. M. Fejer, and M. Loncar, "Ultrahigh-efficiency wavelength conversion in nanophotonic periodically poled lithium niobate waveguides," Optica **5**(11), 1438–1441 (2018).
6. L. Chang, A. Boes, X. Guo, D. T. Spencer, M. J. Kennedy, J. D. Peters, N. Volet, J. Chiles, A. Kowligy, N. Nader, D. D. Hickstein, E. J. Stanton, S. A. Diddams, S. B. Papp, and J. E. Bowers, "Heterogeneously Integrated GaAs Waveguides on Insulator for Efficient Frequency Conversion," Laser Photonics Rev. **12**(10), 1800149 (2018).
7. E. J. Stanton, J. Chiles, N. Nader, G. Moody, G. Moody, N. Volet, L. Chang, J. E. Bowers, S. W. Nam, and R. P. Mirin, "Efficient second harmonic generation in nanophotonic GaAs-on-insulator waveguides," Opt. Express **28**(7), 9521–9532 (2020).
8. N. Poulvellarie, U. Dave, K. Alexander, C. Ciret, M. Billet, C. Mas. Arabì, F. Raineri, S. Combrie, A. De Rossi, G. Roelkens, S.-P. Gorza, B. Kuyken, and F. Leo, "Second Harmonic Generation Enabled by Longitudinal Electric Field Components in Photonic Wire Waveguides," Phys. Rev. A **102**(2), 023521 (2020).

Optics EXPRESS

9. M. Kolesik and J. V. Moloney, "Nonlinear optical pulse propagation simulation: From Maxwell?s to unidirectional equations," Phys. Rev. E **70**(3), 036604 (2004).
10. X. Chen, N. C. Panoiu, and R. M. Osgood, "Theory of Raman-mediated pulsed amplification in silicon-wire waveguides," IEEE J. Quantum Electron. **42**(2), 160–170 (2006).
11. C. Koos, L. Jacome, C. Poulton, J. Leuthold, and W. Freude, "Nonlinear silicon-on-insulator waveguides for all-optical signal processing," Opt. Express **15**(10), 5976–5990 (2007).
12. S. A. Vahid and T. M. Monro, "A full vectorial model for pulse propagation in emerging waveguides with subwavelength structures part I: Kerr nonlinearity," Opt. Express **17**(4), 2298–2318 (2009).
13. B. A. Daniel and G. P. Agrawal, "Vectorial nonlinear propagation in silicon nanowire waveguides: polarization effects," J. Opt. Soc. Am. B **27**(5), 956–965 (2010).
14. L. Alloatti, D. Korn, C. Weimann, C. Koos, W. Freude, and J. Leuthold, "Second-order nonlinear silicon-organic hybrid waveguides," Opt. Express **20**(18), 20506–20515 (2012).
15. K. Alexander, N. A. Savostianova, S. A. Mikhailov, B. Kuyken, and D. Van Thourhout, "Electrically Tunable Optical Nonlinearities in Graphene-Covered SiN Waveguides Characterized by Four-Wave Mixing," ACS Photonics **4**(12), 3039–3044 (2017).
16. D. Duchesne, K. A. Rutkowska, M. Volatier, F. Legare, S. Delprat, M. Chaker, D. Modotto, A. Locatelli, C. De Angelis, M. Sorel, D. N. Christodoulides, G. Salamo, R. Ares, V. Aimez, and R. Morandotti, "Second harmonic generation in AlGaAs photonic wires using low power continuous wave light," Opt. Express **19**(13), 12408–12417 (2011).
17. U. D. Dave, B. Kuyken, F. Leo, S.-P. Gorza, S. Combrie, A. De Rossi, F. Raineri, and G. Roelkens, "eNonlinear properties of dispersion engineered InGaP photonic wire waveguides in the telecommunication wavelength range," Opt. Express **23**(4), 4650–4657 (2015).
18. Y. Ueno, V. Ricci, and G. I. Stegeman, "Second-order susceptibility of $Ga_{0.5}In_{0.5}P$ crystals at $1.5\mu m$ and their feasibility for waveguide quasi-phase matching," J. Opt. Soc. Am. B **14**(6), 1428–1436 (1997).
19. A. Fiore, V. Berger, E. Rosencher, P. Bravetti, and J. Nagle, "Phase matching using an isotropic nonlinear optical material," Nature **391**(6666), 463–466 (1998).
20. L. A. Eyres, P. J. Tourreau, T. J. Pinguet, C. B. Ebert, J. S. Harris, M. M. Fejer, L. Becouarn, B. Gerard, and E. Lallier, "All-epitaxial fabrication of thick, orientation-patterned GaAs films for nonlinear optical frequency conversion," Appl. Phys. Lett. **79**(7), 904–906 (2001).
21. S. Ducci, L. Lanco, V. Berger, A. D. Rossi, V. Ortiz, and M. Calligaro, "Continuous-wave second-harmonic generation in modal phase matched semiconductor waveguides," Appl. Phys. Lett. **84**(16), 2974–2976 (2004).
22. P. S. Kuo, J. Bravo-Abad, and G. S. Solomon, "Second-harmonic generation using -quasi-phasematching in a GaAs whispering-gallery-mode microcavity," Nat. Commun. **5**(1), 3109 (2014).
23. Y. Dumeige and P. Féron, "Whispering-gallery-mode analysis of phase-matched doubly resonant second-harmonic generation," Phys. Rev. A **74**(6), 063804 (2006).
24. C. Mas Arabì, P. Parra-Rivas, C. Ciret, S. P. Gorza, and F. Leo, "Modeling of quasi-phase-matched cavity-enhanced second-harmonic generation," Phys. Rev. A **101**(4), 043818 (2020).
25. A. P. Anthur, H. Zhang, Y. Akimov, J. Ong, D. Kalashnikov, A. I. Kuznetsov, and L. Krivitsky, "Demonstration of second harmonic generationin gallium phosphide nano-waveguides," ArXiv:2001.06142 [Physics] (2020).
26. A. W. Snyder and J. D. Love, *Optical Waveguide Theory* (Chapman and Hall, 1983).
27. D. Vermeulen, K. V. Acoleyen, S. Ghosh, S. Selvaraja, W. De Cort, N. Yebo, E. Hallynck, K. De Vos, P. Debackere, P. Dumon, W. Bogaerts, G. Roelkens, D. Van Thourhout, and R. Baets, "Efficient tapering to the fundamental quasi-tm mode in asymmetrical waveguides," in *ECIO*, (2010), p. paper WeP16.
28. R. W. Boyd, *Nonlinear Optics* (Academic, 2003).
29. H. Kato, S. Adachi, H. Nakanishi, and K. Ohtsuka, "Optical properties of $(Al_xGa_{1-x})_{0.5}In_{0.5}P$ quaternary alloys," Jpn. J. Appl. Phys. **33**(Part 1, No. 1A), 186–192 (1994).
30. U. D. Dave, C. Ciret, S.-P. Gorza, S. Combrié, A. D. Rossi, F. Raineri, G. Roelkens, and B. Kuyken, "Dispersive-wave-based octave-spanning supercontinuum generation in InGaP membrane waveguides on a silicon substrate," Opt. Lett. **40**(15), 3584–3587 (2015).
31. L. Ottaviano, M. Pu, E. Semenova, and K. Yvind, "Low-loss high-confinement waveguides and microring resonators in AlGaAs-on-insulator," Opt. Lett. **41**(17), 3996–3999 (2016).
32. M. Pu, L. Ottaviano, E. Semenova, and K. Yvind, "Efficient frequency comb generation in AlGaAs-on-insulator," Optica **3**(8), 823–826 (2016).
33. M. Parisi, N. Morais, I. Ricciardi, S. Mosca, T. Hansson, S. Wabnitz, G. Leo, and M. D. Rosa, "Single envelope equation modeling of multi-octave comb arrays in microresonators with quadratic and cubic nonlinearities," J. Opt. Soc. Am. B **34**(9), 1842–1847 (2017).
34. J. B. Driscoll, X. Liu, S. Yasseri, I. Hsieh, J. I. Dadap, and R. M. Osgood, "Large longitudinal electric fields (E_z) in silicon nanowire waveguides," Opt. Express **17**(4), 2797–2804 (2009).